Optimization of inhomogeneous magnetization transfer (ihMT) MRI contrast for preclinical studies using dipolar relaxation time (T1D) filtering

V. H. Prevost, O. M. Girard, S. Mchinda, G. Varma, D. C. Alsop, Guillaume Duhamel

Optimization of inhomogeneous Magnetization Transfer (ihMT) MRI contrast for preclinical studies using dipolar relaxation time (T_{1D}) filtering

V.H. Prevost[1], O.M. Girard[1], S. Mchinda[1], G. Varma[2], D.C. Alsop[2] and G. Duhamel[1*]

[1] Aix Marseille Univ, CNRS, CRMBM UMR 7339, Marseille, France
[2] Department of Radiology, Division of MR Research, Beth Israel Deaconess Medical Center, Harvard Medical School, Boston, MA 02215, USA

*** Corresponding Author:**
Guillaume Duhamel, PhD
Aix-Marseille Université
Centre de Résonance Magnétique Biologique et Médicale
CRMBM - CEMEREM, UMR 7339 CNRS - Faculté de Médecine
27 Boulevard Jean Moulin, 13005 Marseille, France
E-mail: guillaume.duhamel@univ-amu.fr

Word counts: 5458

Grant Support:
V.P. received support from the A*MIDEX grant (n°ANR-11-IDEX-0001-02) funded by the French Government "Investissements d'Avenir" program.
S.M received support from IRME 2016

Key words:
Inhomogeneous magnetization transfer, ihMT, dipolar order, dipolar relaxation time, T_{1D}, T_{1D}-filtering, myelin

List of abbreviations:

CC: corpus callosum

cGM: Cortical Grey matter

CM: Cosine-Modulated

Δf: saturation offset frequency

Δt: interpulse delay

E_{tr}: total energy of saturation per repetition time

fc: center of the offset frequency

IC: internal capsule

ihMT/ihMTR: inhomogeneous Magnetization Transfer / inhomogeneous Magnetization Transfer ratio

MT: Magnetization Transfer

Mu: Muscle

PW: Pulse Width

RARE: rapid acquisition with relaxation enhancement

T_{1D}: Dipolar Relaxation Time

WM: White matter

Abstract

Background and Introduction: A pulsed ihMT-prepared fast imaging sequence was implemented at 11.75T for preclinical studies on mouse central nervous system. A strategy based on filtering the ihMT signal originating from short dipolar relaxation time (T_{1D}) components is proposed. It consists in increasing the repetition time of consecutive RF pulses of the dual saturation and allowed improving signal specificity for long T_{1D} myelinated structures. Furthermore, frequency offset, power and timing saturation parameters were adjusted to optimize the ihMT sensitivity.

Results: Optimization of the ihMT sensitivity while preserving strong specificity for the long T_{1D} component of myelinated tissues allowed measurements of ihMT ratios on the order of 4-5% in white matter (WM), 2.5% in grey matter (GM) and 1-1.3% in muscle. This led to high relative ihMT contrasts between myelinated tissues and others (~3-4 between WM and Muscle, and ≥2 between GM and Muscle). Conversely, higher ihMT ratios (~6-7% in WM) could be obtained using minimal T_{1D} filtering achieved with short saturation pulse repetition time or cosine-modulated pulses for the dual frequency saturation.

Conclusion: This study represents a first stage in the process of validating ihMT as a myelin biomarker by providing optimized ihMT preclinical sequences, directly transposable and applicable to other preclinical magnetic fields and scanners. Finally, ihMT ratios measured in various central nervous system areas are provided for future reference.

Introduction

Inhomogeneous Magnetization Transfer (ihMT) is a new endogenous contrast mechanism that has shown great promise for Central Nervous System (CNS) imaging. This technique is based on magnetization transfer (MT), and reveals an interesting characteristic of dipolar-broadened macromolecular lines (1). Human experiments have demonstrated strong capacities of ihMT in discriminating myelinated tissues from others (1–3), with the hypothesis that the lipid membranes, highly present in myelin (4), and which have an inhomogeneously broadened spectrum (5,6), strongly contribute to the ihMT effect. However, the hypothesis of ihMT being a myelin biomarker needs to be further explored and validated. With this perspective, preclinical ihMT MRI applied on well-characterized and established animal models of myelin disorders (demyelination or dysmyelination) will have an important role to play. Potentially being similar to what qMT experiments offer with the *macromolecular proton fraction:* a truly quantitative approach for myelin-sensitive imaging (7–13). A prerequisite to this validation stage is to derive a robust, contrast-optimized and sensitive technique for preclinical ihMT investigations; this constitutes the core of the current work.

The ihMT signal corresponds to the difference in saturation transfer between single frequency-offset and dual frequency-offset saturation performed with the same RF power. A theoretical model for ihMT has been proposed with the inclusion of a dipolar reservoir in the existing two-pool model for MT, which allowed interpreting the inhomogeneous MT signal as a dipolar order effect within motion restricted molecules (14). The name *inhomogeneous MT* was intended to reflect the non-uniform saturation of the spectrum of a line when single frequency off-resonance power is applied. This terminology has been questioned (15), since *inhomogeneous* has been used in the solid-state magnetic resonance literature to indicate

broadening of dipolar systems induced by external factors (16), particularly those permitting hole burning in the spectrum, and separately certain quantum properties of the system under magic angle spinning (17). In contrast, the basic underlying physical model of the ihMT effect, which relies on dipolar order theory (14), is generally accepted (15,18). For lack of an obviously more specific name and for consistency with the prior literature on ihMT, we retain the name inhomogeneous MT and use the word *inhomogeneous* to reflect lines whose spectrum can be non-uniformly saturated with single-offset RF.

Dipolar order may in principle be encountered in various tissue structures, providing that averaging is slowed down by motional restriction. Dipolar order is characterized by a dipolar relaxation time, $T_{1D,}$ and its associated fraction, f within the bound pool. In the framework of ihMT, the finite lifetime of the dipolar order, i.e. T_{1D}, indicates the duration of the homogenization process within the line. Long T_{1D} values associated with a large fraction of the semi-solid pool are responsible for the highest ihMT ratio (ihMTR) obtained in myelinated WM structures. It is however possible to reveal ihMT signals in very short T_{1D} tissues when using high saturation power levels. This property has not been fully appreciated in our previous human studies (1,3) because these were focused on areas of interest located in the brain and relatively low power intensities were used, as imposed by regulatory energy deposition limitations. Conversely, preliminary studies performed on mice using high power levels have evidenced a non-negligible ihMT signal in muscle (19) and *in vitro* studies also revealed non-zero ihMT signal in short T_{1D} components such as wood or hair (15). In this context it is appropriate to envision ihMT as a T_{1D}-weighted imaging modality, for which various contrast regimes and tissue sensitivity could apply.

In this study, we introduced the concept of *T_{1D}–filtered ihMT* imaging and used it to optimize the contrast of preclinical ihMT images, obtained on mice at 11.75T using a 2D pulsed ihMT fast imaging sequence (1,3). The dual saturation scheme was adjusted to vary

the T_{1D} weighting in order to remove the ihMT signal contribution from a certain range of low T_{1D}s while maintaining signal from the longer T_{1D}s components. This T_{1D}–filtering concept was first illustrated *in vitro* on phantoms and further used *in vivo* to attenuate the ihMT signal of the shorter T_{1D} muscle components, while preserving high signal from long-T_{1D} myelinated structures, overall enhancing the contrast of ihMT for these particular structures. Optimization of the ihMT sensitivity was achieved by adjustment of the saturation frequency offset and the other RF timing and power parameters. Finally, the resulting optimized T_{1D}-filtered sequence was used to establish a reference database of ihMTR values in normal mouse CNS along with relative ihMT contrast values between various structures.

Material & Methods

Animal experiments

Animal studies were conducted in agreement with the European Council Directive 2010/63/EU, the French guidelines for animal care from the French Department of Agriculture (Animal Rights Division), and approved by our institutional committee on Ethics in animal research. After isoflurane induction in an anesthetic chamber at 3%, healthy female C57Bl/6J mice (10-20 weeks, 23±2g) were maintained under anaesthesia by spontaneous respiration of a mixture of air and isoflurane (1.5%, constant flow 300mL/min, Univentor 400 anesthesia unit, Zejtun, Malta), through a dedicated nose cone. Respiration and temperature were controlled throughout the experiment with a MR compatible monitoring and gating system (SA Instruments, Stony Brook, NY). A heating blanket connected to a water bath system was placed on the mice's back to maintain physiological temperature throughout the whole experiments (T=37.0±0.5°C).

MR setup

In vivo experiments were performed on a preclinical 11.75T scanner (Bruker Avance 500 MHz/89 mm wide bore vertical imager, Ettlingen, Germany) with a transmit/receive volume birdcage coil (Bruker, Ettlingen, Germany; length L=30 mm, diameter Ø=20 mm). Prior to ihMT data acquisition, first and second order shimming was achieved using the Bruker Fastmap procedure in a 11.5x11.5x11.5 mm^3 3D volume covering the entire mouse brain. B_0 maps were then acquired using the Bruker FieldMap procedure, based on the acquisition of a 3D double gradient echo dataset (TE_1/TE_2=1.5/5.5ms, matrix 96x64x64, FOV 30x20x20 mm^3).

Pulsed ihMT sequence

The ihMT signal generation relies on the comparison of two different MT weighted images (1): one using a single frequency-offset (+Δf), leading to the saturated image MT^+, and the other using a dual frequency-offset (+Δf and –Δf) using identical total energy, leading to the saturated image MT^{+-}. In order to compensate for MT asymmetry effects, two additional single (MT^-) and dual (MT^{-+}) frequency-offset acquisitions are acquired so that the final ihMT image is generated by the following combination:

$$ihMT = MT^+ + MT^- - MT^{\pm} - MT^{\mp} \qquad \text{Equation 1}$$

At ultra-high magnetic field strength, efficient correction of MT-asymmetry signal contributions also requires the frequency offsets Δf to be applied relative to a frequency center, *fc*, slightly shifted to *fc=-100Hz* from the free water resonance frequency (19). The ihMT ratio is defined by ihMTR = ihMT/S_0, where S_0 is the signal measured with RF saturation power set to zero.

A pulsed ihMT preparation module similar to that previously described for human studies (3) was implemented under Bruker Paravision 5.1 software (Fig 1). The saturation was achieved with a pulse train consisting of several frequency-shifted Hann-shaped pulses (duration *PW*) repeated every Δt during a total saturation duration τ (total number of pulses given by $\tau/\Delta t$), and which deposited a total RF energy proportional to E_{TR}, with $E_{TR} = B_{1,RMS(p)}^2 \times \tau \times \frac{PW}{\Delta t} = B_{1,RMS}^2 \times \tau$ (in $\mu T^2 \bullet s$). $B_{1,RMS(p)}$ is the root mean square B_1 calculated over a single pulse and $B_{1,RMS}$ is that calculated over the whole saturation period. Crusher gradients were inserted between saturation pulses.

Single frequency-offset saturation MT^+ *or* MT^- images were acquired with the frequency of all the saturation pulses applied at $+\Delta f$ or $-\Delta f$ respectively (Fig 1a). Dual frequency-offset saturation $MT^{+/-}$ ($MT^{-/+}$) images were obtained either by using cosine-modulated (CM) Hann-shaped pulses (Fig 1b) or by alternation of the frequency of consecutive pulses (Fig 1c).

MR imaging

A 2D single-slice single-shot fast imaging readout (RARE - rapid acquisition with relaxation enhancement) was used following the pulsed ihMT preparation with the imaging parameters: 1 mm slice thickness, 20 mm field of view (FOV) and 64x64 image matrix (pixel resolution of 0.31x0.31 mm^2), min TE and echo spacing 1.82 ms, TE_{eff}=12.74 ms, RARE factor=38, partial Fourier acceleration=1.7, linear phase encoding, bandwidth=400 kHz, TR=3s. The acquisition train length was ~70 ms. Imaging was performed in the axial direction for the studies dedicated to the investigation of the saturation parameters.

Post-processing

Magnitude data were processed using Matlab (vR2012, The MathWorks Inc., Natick, MA) custom routines. Mean ihMT and MT ratios (*ihMTR* as defined above and $MTR=1-MT^{+}/S_0$) and standard deviations of the mean ratios calculated across animals were measured in Regions-Of-Interest (ROIs) selected in both brain hemispheres in several WM and GM areas, including the internal capsule (IC), the corpus callosum (CC) and cortical gray matter (cGM). A ROI was also selected in the muscle (Mu) area in order to assess the ihMT specificity for myelinated tissues relative to a reference short-T_{1D} unmyelinated structure. See Fig 3a for the ROI localization. Relative *ihMTR* contrasts (defined as the ratios of the *ihMTR* values measured in two distinct structures) and contrast-to-noise (CNR) ratios (defined as the difference of ihMT signals between two structures divided by the noise of the ihMT image) were also evaluated for specificity considerations.

Principle of T_{1D}-filtered ihMT imaging

By comparing a single frequency-offset MT image, whose expression contains a term related to T_{1D} (Eq. 10 of (14)) with a dual frequency-offset MT image, whose expression is free of any T_{1D} contribution (Eq. 6 of (14)), the dipolar contribution is isolated from traditional MT and is revealed in the ihMT signal combination. In other words, dipolar order effects associated to non-trivial T_{1D} components (i.e. $T_{1D} \neq 0$) are created with single offset RF saturation, whereas they are ideally constrained to zero with a perfect dual offset RF saturation. Sensitivity of the ihMT signal to T_{1D}s can hence be adjusted by modulating the efficiency of the dual frequency-offset saturation. This latter may be performed in two different ways (1): 1) using a cosine-modulated envelope for the shaped MT pulses, which corresponds to a simultaneous saturation at both frequency bands (Fig 1b); and 2) using a frequency alternated pulsed approach for which each frequency offset is excited sequentially (Fig 1c). The first approach may be considered as a genuine dual frequency-offset saturation

for which the dipolar order is actually decoupled from the Zeeman order (14), hence providing the largest signal difference with the single frequency saturation experiment, and leading to strong ihMT signal. Alternatively, the second approach, which approximates a dual frequency-offset saturation, adds an extra degree of freedom corresponding to the time between two consecutive pulses (Δt) at alternated frequency offsets. In the following, Δt is referred to *switching time*. When the switching time increases, the ihMT signal decays (Fig 5f of (19)) because of T_{1D} relaxation. For the sake of illustration, in the limiting case where this switching time increased towards infinity, the "dual-frequency" saturation scenario would become equivalent to the single-frequency one and the ihMT signal would naturally vanish. In a separate work, we reported a theoretical model for this decay, which combined with a modified version of the dual saturation, based upon the insertion of several pulses at one frequency before alternating to the opposite one, allowed *in vivo* estimations of T_{1D} values (20). Here instead, for T_{1D}-filtered ihMT imaging, we used a dual saturation scheme with single pulse at alternating frequency (Fig 1c) and adapted switching time, Δt. Increasing the switching time, Δt, increases the time at which the dual-offset saturation could be considered effective. Hence, fixing Δt should allow T_{1D}-weighting of the ihMT signal, by reducing the ihMT signal of components with $T_{1D}<\Delta t$. Conversely, when the dual-frequency saturation is achieved by means of cosine-modulated pulses (length *PW,* Fig 1b), the ihMT signal is sensitized to shorter T_{1D} value components and minimal T_{1D}-filtering is achieved.

T_{1D}-filtered ihMT imaging was illustrated *in vitro* on a phantom composed of hair conditioner (*Le petit Marseillais*®) (*hc*) and agarose 4% (*ag4%*). Hair conditioners, whose major components are suspensions of fatty alcohols, which form lamellar structures of methylene chains (21) have shown strong ihMT effects. Whereas no conclusion regarding neuroimaging can be derived from ihMT experiments on hair conditioners, these latter can be advantageously used for technical set up and adjustment purposes (1). T_{1D} values of *hc* and

agarose 4% were estimated to T_{1D}=16.1±6.0ms and to T_{1D}=1.6±0.3ms respectively, by fitting experimental data to an extended ihMT normalized model as outlined in (20). A single Δt value *(Δt =1.3ms)* was used for dual frequency-offset saturation performed with cosine-modulation for which no T_{1D} filtering is expected, and Δt =1.3ms, 2.3ms, 3.3ms, 4.3ms, 5.3ms and 7.3ms were used for dual frequency-offset saturation performed with alternating pulses. Other ihMT saturation parameters were: Δf=±10kHz, PW=1ms, $B_{1,RMS}$=6.7μT and τ=0.9s leading to E_{TR}=40$\mu T^2.s$. Experiments were conducted at 25°C.

In vivo experiments

Optimizing the ihMT contrast with T_{1D}-filtering imaging

Values of T_{1D} in mouse tissues were estimated with the technique outlined in (20) to T_{1D}=6.1±0.8ms in internal capsule, T_{1D}=5.6±1.2ms in cortical gray matter, and T_{1D}=2.2±0.6ms in muscle. The proposed T_{1D}-filtering strategy was thus used to attenuate the ihMT signal of the shorter T_{1D} components, represented by muscle here, while preserving high amount of signal of long-T_{1D} WM and GM, overall optimizing the contrast of ihMT for these myelinated structures. *In vivo* T_{1D} filtering was performed on 3 mice with the same parameters as those used for phantom experiments. Thirty averages (NEX=30) per tested parameter value (acquisition time ~ 8 minutes) were acquired in order to increase the signal-to-noise.

Optimizing the ihMT sensitivity

This experiment was performed on 3 mice and the dual-frequency offset saturation was achieved with the frequency alternated pulsed approach (Fig 1c). The effects of all the relevant parameters for ihMT preparation, i.e. frequency offset (Δf), timing parameters (*PW,*

Δt and t) and RF power of the ihMT saturation, were investigated. The range of tested parameters was limited to: 6kHz ≤ Δf ≤ 20kHz, 1ms ≤ PW ≤ 3ms, 1.3ms ≤ Δt ≤ 3.3ms and $5\mu T^2.s \leq E_{TR} \leq 58\mu T^2.s$. These E_{TR} values were achieved either by varying $B_{1,RMS}$ ($2.4\mu T \leq B_{1,RMS} \leq 7.4\mu T$) at fixed total saturation time (τ=0.9s) or conversely, by varying τ ($0.25s < \tau < 1.3s$) at fixed $B_{1,RMS}$ ($B_{1,RMS}$=6.7μT). Note that for experiments performed at variable τ, a TR of 9s (i.e. full-relaxation conditions) was used. In order to evaluate the effect of a given parameter, it was varied independently whilst keeping the other parameters constant. All sets of parameters examined are reported in table 1 and were acquired with 30 NEX (acquisition time ~ 8 minutes per tested parameter value).

Reference ihMTR measurements in mouse CNS

Following the previous sensitivity and specificity characterization, reference 2D ihMT RARE images, with alternating pulses for dual frequency-offset saturation were sequentially acquired in coronal, axial (2 slices) and sagittal directions on 4 mice with Δf=±10kHz, PW=3ms, Δt=3.3ms, $B_{1,RMS}$=6.7μT, τ=0.9s and E_{TR}=40 $\mu T^2.s$. IhMT images were averaged 180 times (NEX=180, total acquisition time ~45 minutes) to improve SNR. This experiment allowed the establishment of a reference database of ihMTR/MTR values in trigeminal nerves (TN), brain white matter (internal capsule – IC, fornix – Fo, corpus callosum – CC, fimbria – Fi, cerebellum – Ce, external capsule – EC), brain gray matter (colliculi – Co, striatum – CPU, cortex – cGM), brain mixed structure (brain stem – BS, thalamus – Tha) and spinal cord gray and white matter (SCGM, SCWM). See Fig 6 for the ROI localization.

Results

Principle of T_{1D}-filtered ihMT imaging

Principle of T_{1D}-filtered ihMT imaging is illustrated *in vitro* in Figure 2, which shows ihMT images (Fig 2a) and variations in ihMTR (Fig 2b) measured in hc *(*long T_{1D}^{hc}~16ms) and ag4% (short $T_{1D}^{ag4\%}$~1.6ms) for different values of Δt. For short and long T_{1D} components, the use of cosine-modulated pulses (i.e. simultaneous dual frequency-offset saturation) resulted in the highest ihMTR values (Fig 2b, $ihMTR^{hc}$=42% and $ihMTR^{ag4\%}$=3.4%). T_{1D}-filtering of the ihMT signal was evidenced in the dynamics of ihMTR with increasing Δt when using alternating pulses for dual frequency-offset saturation: ihMTR values of the short-T_{1D} ag4% reduced to $ihMTR^{ag4\%}$=2.7% at $\Delta t=1.3ms$, were further divided by a factor greater than 2 at $\Delta t=3.3ms$ ($ihMTR^{ag4\%}$=1.1%) and tended towards zero for longer Δt values ($ihMTR^{ag4\%}$<0.5% for $\Delta t>4.3ms$). Conversely, for the long-T_{1D} hc, the studied variation of Δt had lower effect on the ihMTR values: $ihMTR^{hc}$=41% at $\Delta t=1.3ms$, $ihMTR^{hc}$=38% at $\Delta t=3.3ms$ and $ihMTR^{hc}$=32% at $\Delta t=6.3ms$.

In vivo optimization of the ihMT contrast with T_{1D}-filtering imaging

In vivo T_{1D}-filtered ihMT imaging is highlighted in Figure 3, which shows a mouse brain T_{1D} map (Fig 3a), ihMTR maps for different Δt values (Fig 3a) and the corresponding ihMTR values measured in IC, cGM and Mu (Fig 3b). Similarly to *in vitro* experiments, higher ihMTR values were obtained when the dual frequency-offset saturation was performed with cosine-modulated pulses yielding to $ihMTR^{IC}$=7.5%, $ihMTR^{cGM}$=4.2% and $ihMTR^{Mu}$=3.8%. This corresponded to relative ihMTR contrast ratios of ~1.8 between IC and cGM, of ~2.0 between IC and Mu and of ~1.1 between cGM and Mu (Fig 3c). For the alternating dual frequency saturation implementation, ihMTR values decreased with increasing Δt (Fig 3b), but the relative ihMTR contrast between myelinated and non-myelinated structures was

enhanced (Fig 3c), as a consequence of stronger T_{1D} –weighting introduced with longer T_{1D} values (Fig 3a). In particular, Δt values ≥3.3ms allowed filtering of the ihMT signal in muscle ($ihMTR^{Mu}$ ≤1%, T_{1D}^{Mu}=2.2±0.6ms), hence reinforcing the relative IC/Mu and cGM/Mu contrasts (Fig 3a, blue and black curves of Fig 3c). The relative contrast between IC and cGM was relatively insensitive to Δt variations, as illustrated by little changes in the IC/cGM ihMTR ratios (~ 2) with increasing Δt (Fig 3c, red curve). Contrast-to-noise ratios measured between the same structures (Fig. 3d) showed moderate decrease for Δt≤3.3ms, and a big drop for Δt>3.3ms. These results suggested that when T_{1D}-filtering is necessary, Δt=3.3ms represents a good configuration for enhancing the contrast between myelinated structures and others. With these settings relative ihMTR contrast ratios of ~5.0 for IC/Mu and ~2.3 for cGM/Mu were obtained with a reduced loss of sensitivity in mouse brain ($ihMT^{IC}$=(5.0±0.1)%, $ihMT^{cGM}$=(2.3±0.2)%). If one is interested by WM/GM contrast analysis and not concerned with muscle signal, then Δt of 1.3ms may be more appropriate, offering higher CNR and higher ihMTR values.

Optimizing the ihMT sensitivity

The sensitivity of ihMT as a function of Δf, PW, Δt, $B_{1,RMS}$ and τ is reported in Figs. 4-5. Variation of ihMTR with frequency offset in myelinated tissue provided bell-shaped curves with maximum values obtained at different Δf values depending on the brain tissue (Fig 4a-c). For a saturation power of $B_{1,RMS}$=6.7μT, maximum ihMTR values were obtained at Δf =10kHz for IC, at Δf =10-12kHz for cGM, and at Δf =12kHz for CC. For muscle (Fig 4d), the maximum occurred for Δf>18kHz. Interestingly, for all structures, the frequency offset corresponding to the maximum ihMTR value tended to shift to higher values when the saturation power increased (e.g. in IC: for $B_{1,RMS}$=5.1μT, $ihMTR^{max}$=4.5% at Δf=8-10kHz, for

$B_{1,RMS}$=6.7μT, ihMTR^{max}=5.2% at Δf =10kHz and for $B_{1,RMS}$=8.4μT, ihMTR^{max}=5.3% at Δf =12kHz). These results suggested that Δf values of ~10-12kHz and saturation power $B_{1,RMS}$ ≥6.7μT can maximize the ihMT signal in WM/GM structures while maintaining a low value in muscle.

At fixed $B_{1,RMS}$, little difference was observed in ihMTR values for increasing PW and constant Δt (Fig 5a), whereas ihMTR values clearly decreased when increasing Δt (Fig 5b), again confirming the role of Δt as a determinant of T_{1D} filtering.

In WM and GM, ihMTR values tended to saturate for $B_{1,RMS}$≥6μT, whereas in Mu, they kept increasing with increasing $B_{1,RMS}$ (Fig 5c). For increasing τ and fixed $B_{1,RMS}=6.7\mu T$, ihMTR values reached their maximum for τ~900ms and further slightly decreased for τ>1000ms (Fig 5d).

Reference T_{1D}-filtered ihMTR measurements in mouse CNS

Figure 6 shows typical MTR maps (left column) and ihMTR maps (right column) (NEX=180) obtained in axial, coronal and sagittal directions with optimized parameter settings: $\Delta f=\pm 10kHz$, $PW=3ms$, $\Delta t=3.3ms$, $B_{1,RMS}=6.7\mu T$, $E_{TR}=40\ \mu T^2.s$ and $\tau=0.9s$. A reference database of ihMTR and MTR values in CNS structures measured in such images (location indicated in MT$^+$ images, Fig 6 middle column) is presented in table 2 and the relative ihMTR contrasts calculated between all structures are reported in table 3.

Discussion

This study aimed at optimizing the contrast and the sensitivity of ihMT in the context of preclinical investigations of the mouse CNS using T_{1D}-filtering strategy in combination with adapted saturation parameters.

The variations of ihMTR with changes in Δf (Fig 4), $B_{1,RMS}$ (Fig 5c) and τ (Fig 5d) in the different mouse brain structures are in good agreement with theoretical expectations. In particular, both the ihMTR bell-shape curves shifting to higher Δf values when increasing $B_{1,RMS,}$ the trend of ihMT signal saturation at high $B_{1,RMS}$ and the decrease of ihMTR values for long saturation time τ, were predicted by the theoretical model (14). However, experimental data showed that the saturation of ihMT signal started at lower $B_{1,RMS}$ values ($B_{1,RMS}>6\mu T$) than those predicted by the simulations ($B_{1,RMS}\geq 10\mu T$). $B_{1,RMS}$ values at which saturation occurred in experiments corresponded to root-mean-square pulse powers $B_{1,RMS(p)}$ of $\sim 7\mu T$ and higher. These results are in agreement with those previously reported on humans with a similar ihMT sequence (Fig 6 in (3)), which showed saturation of the ihMT signal in human WM/GM for $B_{1,RMS(p)}$ values as high as $\sim 8\mu T$. Further support for ihMT signal saturation at high RF pulse power was highlighted in Fig 5a, which showed little difference in ihMTR for fixed $B_{1,RMS}$ when varying PW, and hence upon varying $B_{1,RMS(p)}$. The apparent mismatch between the current theoretical model prediction and the experimental results strongly suggests that the instantaneous RF power deposition occurring during PW should be taken into account to refine the ihMT model, and should lead to more accurate prediction of the ihMT signal behavior vs. sequence parameters. Consideration of this factor should also allow investigating new strategies of power deposition in order to further optimize the ihMT sensitivity.

The variations of ihMTR with Δf values obtained in this study (Fig 4) provided additional support for an effect of the angular orientation of white matter relative to the main magnetic field. This was suggested in our previous studies and illustrated by an ihMT signal only visible in the corpus callosum (axons lying mainly perpendicular to the magnetic field) at high frequency offset (Δf=21kHz) (1,14). Here, the steeper decrease of ihMTR with Δf in IC

(axons lying mainly parallel to B_0) compared to that in CC resulted in similar ihMTR values for Δf=20kHz, further suggesting that above this frequency offset, inversion will occur and ihMTR values will be higher in CC. Previous MT experiments also reported a dependence of qMT derived parameters (e.g. T_{2B} - T_2 of bound protons) with white matter anisotropy (22,23). Hence, the results obtained here warrant further investigations in order to interpret the white matter anisotropy effect on ihMT and evaluate to what extent it is a potential confound for ihMT quantification.

Absolute ihMTR values in mouse brain and spinal cord WM measured in this study were ~1.5-2 times smaller than those reported in humans at 1.5T in similar structures (2,3). The low resolution used in this study, and consequential partial volume effects, might have led to underestimated values, thus explaining, at least in part, these differences. Given that identical ihMT MR sequences were used for humans and animal studies and that, slightly higher ihMTR values would be expected at higher magnetic field strength due to longer T1s (Fig. S1), the reasons for lower ihMTR values could be related to physiological differences between species. The mouse WM dipolar relaxation time T_{1D} is only slightly shorter than that of human (T_{1D}~6.1ms vs T_{1D}~6.3ms) whilst the measured fraction f of the bound pool with dipolar order is almost halved (20). This suggests differences in the composition and/or the structure of the WM compounds to which ihMT is sensitive. The rich-lipid composition (70% lipids, 30% proteins) (24) and unique structure (molecular lipid-bilayer membrane tightly wrapped around axons) of myelin, which constitutes 40-50% of white matter, is thought to favor the ihMT effect. Similarities in the composition of myelin main lipids were found between mammalian species with a few exceptions (4). Thus, whereas both human myelin and mouse myelin have similar cholesterol content (~27% of total myelin lipids) and comparable galactolipids (cerebroside and sulfatide, ~27% of total lipids), differences in phospholipid content (~45% of total lipids) were noticed. In particular, mouse myelin has 2-3

times less sphingomyelin but more phosphoglycerides than human myelin (25–27). Sphingomyelin and other sphingolipids (cerebrosides, sulfatides) mainly contain long-chain (>19 carbon atoms) saturated fatty acids (28), which contribute to a closely packed, highly stable membrane structure. In contrast, numerous mid-chain (<19 carbon atoms) unsaturated fatty acids present in phosphoglycerides contribute to a more loosely packed, less stable structure due to weaker binding interactions between neighboring molecules (29). Less sphingomyelin and more phosphoglycerides may lead to higher fluidity properties of the mouse myelin structure, which could favor the mechanisms of spectral homogenization of the corresponding broadened lines and thus reduce ihMT effects. Another major difference between human and mouse experiments are the use of anaesthetics, which may induce changes in myelin structure (30), and hence affect the ihMT signal. Performing ihMT phantom experiments on lipid components of myelin (31) and *in vivo* on animal models with deficiency of myelin lipids (25,26) would help in validating/invalidating these hypotheses.

Although this study did not address the source of ihMT contrast, it confirms that most components with non-trivial T_{1D} can be revealed by the ihMT technique (14,15), provided that the saturation parameters are appropriately chosen. In the original ihMT paper (1), with an experimental design slightly different than that of this study, we concluded that dual saturation achieved by cosine-modulated pulses or alternated pulses approach yield similar metrics. However the present study demonstrated that both approaches are essentially different, addressing different tissue components, and measuring potentially different metrics. Hence, simultaneous dual frequency-offset saturation approach by means of cosine-modulated pulses provided significant ihMT signal in short T_{1D} components such as muscle (T_{1D} ~1.6ms), suggesting that this strategy could enable *in vivo* studies of ihMT in tissues other than those found in CNS. Conversely, alternating pulses for dual saturation enables T_{1D}-filtered ihMT imaging, which can be exploited to enhance the contrast between tissues with

different T_{1D} values. This may be seen similar to T_2-weighting imaging achieved with increase of the echo time of spin-echo based sequences and used to filter the signal of short T_2 components. Here, the short-T_{1D} muscle signal was filtered by means of increase of the repetition time between consecutive RF pulses of the dual saturation, thereby optimizing the contrast for longer T_{1D} myelinated WM and GM structures (Fig 3a).

One important finding derived from experiments using alternating pulses for dual saturation is that, whereas absolute ihMTR values in CNS changed with saturation parameters, the relative WM/GM ihMTR contrasts were particularly robust to them, as illustrated by the little differences observed between the ratios of WM/GM ihMTR values (~2) measured over the whole range of investigated saturation parameters. Of particular interest, this relative ihMTR contrast of ~2 associated with a low sensitivity to T_{1D}-filtering when increasing Δt (Fig 3c, red curve), supports the close WM and GM T_{1D} values estimated *in vivo* (T_{1D}^{IC}=*6.1±0.8ms*, T_{1D}^{cGM}=5.6±1.2*ms*) (20) and is consistent with associated fractions of bound pool, *f*, almost doubled in WM compared to that in GM (14). In other words, the bound pool fraction associated to the long T_{1D} of brain tissue is the dominant source of ihMTR contrast between WM and GM. These results however differ with measurement from a recent study, which found shorter T_{1D} values in GM compared to WM using a Jeener-Broekaert echoes (18) technique applied on a fixed bovine spinal cord. T_{1D} in fixed tissue specimens may differ from *in vivo* values. One should also note that unlike the Jeener-Broekaert echoes technique, which estimates T_{1D} values based on the superposition of decay of all components, the fitting technique used for *in vivo* measurements (20) is biased towards long values as components with short T_{1D} are filtered before signal acquisition. GM T_{1D} could be composed of a long T_{1D} component correctly estimated by the fitting technique, and a short T_{1D} component filtered by the fitting technique. The robustness of relative ihMTR contrasts in brain to experimental settings may be particularly advantageous as assessment of the

quantitative pair of parameters $\{T_{1D}, f\}$ (which requires acquisitions at different frequency offsets and power levels (14) and potentially dual frequency switching times) may not be required for practical characterization of CNS tissues with ihMT. For that purpose, the use of short Δt values or in the limiting case of the cosine modulated approach, would have the advantage of providing higher ihMTR and CNR values (Figs. 3b,d). However, one should notice that this would sensitize the ihMT images to shorter T_{1D} value components, thereby potentially modifying the source of contrast as compared to T_{1D}-filtered conditions. Signs of this effect can be seen with the use of CM for dual saturation. The lower relative WM/GM contrast value (~1.8 v.s 2 for alternated pulses) seems to indicate that short T_{1D} components participate more to the GM ihMT signal compared to that of WM. Overall this opens the questions of the specificity of ihMT signal and its relationship with myelin. Further studies will address this question by looking for correlations between relative ihMTR contrasts (and/or ihMTR values) and gold standard myelin density measurements such as assessed by quantitative histology. In this context, the strong similarities between the ihMTR maps obtained in this study (Fig 6) and the bound pool fraction maps in rat brain, derived from qMT experiments, and which has been shown to correlate with myelin density maps (13), are very promising.

More generally, the reinforced contrast for WM structures obtained with ihMT at 11.75T are of very significant importance in the context of high-magnetic field preclinical imaging, where more common myelin-sensitive techniques such as T1-weighted imaging or standard-MT based imaging (32) tend to lose contrast(33–35) due to uniform increases in T1 values of brain structures (36). Contrast-enhanced strategies by injection of gadolinium or manganese have been proposed for improving the mapping of myelin-rich WM structures using MT MRI at high magnetic field (37,38). Quantitative maps of the bound pool fraction extracted from multi-parametric qMT methods provide similar brain tissue contrast to that of

ihMT, but at the cost of time-consuming experiments and/or more sophisticated post-processing (13,39). From a practical point of view and compared to qMT experiments, the implementation of ihMT described in this study suffers from low time efficiency, low spatial resolution and limited volume coverage. However strategies for 3D ihMT imaging have already been developed for humans (40,41) and can be duplicated for preclinical investigations. The ihMT contrast is preserved at high magnetic field as its underlying mechanisms are related to dipolar order effects within bound molecules, which do not scale directly with B_0. Hence, the relationship between ihMTR and the saturation parameters is mostly independent of field strength, even though a slight increase of absolute ihMTR values can be observed when magnetic field increases due to T_1 increase of free water protons (Fig. S1). Since preclinical scanners typically operate in a closer range of magnetic field strengths ($7T<B_0<11.75T$), differences in absolute ihMTR related to magnetic field strengths should be reduced, overall making the contrast/sensitivity optimization results of the current study highly reproducible, and directly transposable and applicable to other preclinical magnetic fields and scanners. Finally, a practical advantage of ihMT and its pronounced contrast features could be its potential for automatic brain structure extraction. For example, with the parameter set corresponding to Fig. 6, a 3.5-threshold of ihMTR values would mask all structures except WM ones. Such potential may further facilitate automatic whole-brain measurements and eliminate time-consuming manual image analysis in serial high-volume small animal studies.

Conclusions

A 2D pulsed ihMT prepared fast imaging sequence was implemented at 11.75T for preclinical studies on mouse CNS. A strategy based on filtering the signal of short T_{1D} components and achieved by proper tuning of the repetition time between consecutive RF pulses of the dual saturation was used to optimize the ihMT contrast for long T_{1D} myelinated structures.

Furthermore frequency offset, power and timing saturation parameters were adjusted to optimize the ihMT sensitivity, providing measurements of ihMTR in mouse CNS for future reference. Typical ihMTR values on the order of 4-5% in WM, 2.5% in GM and 1-1.3% in muscle were obtained, thus leading to high positive relative ihMTR contrasts between myelinated tissues and other tissues (~3-4 between WM and Mu, and ≥2 between GM and Mu). Of particular importance, the relative ihMTR contrast between WM and GM (~ 2) appeared to be relatively independent of the saturation parameters, supporting similar T_{1D} values in both brain structures. Hence, for WM/GM analyses minimizing T_{1D}-filtering by using short Δt value (e.g. Δt=1.3ms) may be a good option, offering higher CNR and higher ihMTR values. These results are of great significance and represent a first milestone in the process of validating ihMT as a biomarker of myelin.

References

1. Varma G, Duhamel G, de Bazelaire C, Alsop DC. Magnetization transfer from inhomogeneously broadened lines: A potential marker for myelin: Magn. Reson. Med. 2015;73:614–622. doi: 10.1002/mrm.25174.

2. Girard OM, Callot V, Prevost VH, Robert B, Taso M, Ribeiro G, Varma G, Rangwala N, Alsop DC, Duhamel G. Magnetization transfer from inhomogeneously broadened lines (ihMT): Improved imaging strategy for spinal cord applications: ihMT for Spinal Cord Applications. Magn. Reson. Med. 2016:n/a-n/a. doi: 10.1002/mrm.26134.

3. Girard OM, Prevost VH, Varma G, Cozzone PJ, Alsop DC, Duhamel G. Magnetization transfer from inhomogeneously broadened lines (ihMT): Experimental optimization of saturation parameters for human brain imaging at 1.5 Tesla. Magn. Reson. Med. 2015;73:2111–21. doi: 10.1002/mrm.25330.

4. Morell P. Myelin. Springer US; 2013.

5. Davis JH, Auger M, Hodges RS. High resolution 1H nuclear magnetic resonance of a transmembrane peptide. Biophys. J. 1995;69:1917.

6. Chen J-H, Sambol EB, DeCarolis P, O'Connor R, Geha RC, Wu YV, Singer S. High-resolution MAS NMR spectroscopy detection of the spin magnetization exchange by cross-relaxation and chemical exchange in intact cell lines and human tissue specimens. Magn. Reson. Med. 2006;55:1246–1256. doi: 10.1002/mrm.20889.

7. Dula AN, Gochberg DF, Valentine HL, Valentine WM, Does MD. Multiexponential T2, magnetization transfer, and quantitative histology in white matter tracts of rat spinal cord. Magn. Reson. Med. Off. J. Soc. Magn. Reson. Med. Soc. Magn. Reson. Med. 2010;63:902–909. doi: 10.1002/mrm.22267.

8. Ou X, Sun S-W, Liang H-F, Song S-K, Gochberg DF. The MT pool size ratio and the DTI radial diffusivity may reflect the myelination in shiverer and control mice. NMR Biomed. 2009;22:480–487. doi: 10.1002/nbm.1358.

9. Ou X, Sun S-W, Liang H-F, Song S-K, Gochberg DF. Quantitative magnetization transfer measured pool-size ratio reflects optic nerve myelin content in ex vivo mice. Magn. Reson. Med. 2009;61:364–371. doi: 10.1002/mrm.21850.

10. Rausch M, Tofts P, Lervik P, Walmsley A, Mir A, Schubart A, Seabrook T. Characterization of white matter damage in animal models of multiple sclerosis by magnetization transfer ratio and quantitative mapping of the apparent bound proton fraction f. Mult. Scler. 2009;15:16–27. doi: 10.1177/1352458508096006.

11. Samsonov A, Alexander AL, Mossahebi P, Wu Y-C, Duncan ID, Field AS. Quantitative MR imaging of two-pool magnetization transfer model parameters in myelin mutant shaking pup. NeuroImage 2012;62:1390–1398. doi: 10.1016/j.neuroimage.2012.05.077.

12. Turati L, Moscatelli M, Mastropietro A, et al. *In vivo* quantitative magnetization transfer imaging correlates with histology during de- and remyelination in cuprizone-treated mice: QUANTITATIVE MAGNETIZATION TRANSFER IMAGING IN CUPRIZONE-TREATED MICE. NMR Biomed. 2015;28:327–337. doi: 10.1002/nbm.3253.

13. Underhill HR, Rostomily RC, Mikheev AM, Yuan C, Yarnykh VL. Fast bound pool fraction imaging of the in vivo rat brain: Association with myelin content and validation in the C6 glioma model. NeuroImage 2011;54:2052–2065. doi: 10.1016/j.neuroimage.2010.10.065.

14. Varma G, Girard OM, Prevost VH, Grant A, Duhamel GD, Alsop DC. Interpretation of magnetization transfer from inhomogeneously broadened lines (ihMT) in tissues as a dipolar order effect within motion restricted molecules. J. Magn. Reson. 2015;260:67–76. doi: 10.1016/j.jmr.2015.08.024.

15. Manning AP, Chang KL, MacKay AL, Michal CA. The physical mechanism of "inhomogeneous" magnetization transfer MRI. J. Magn. Reson. San Diego Calif 1997 2016;274:125–136. doi: 10.1016/j.jmr.2016.11.013.

16. Portis AM. Electronic structure of F centers: Saturation of the electron spin resonance. Phys. Rev. 1953;91:1071.

17. Maricq MM, Waugh JS. NMR in rotating solids. J. Chem. Phys. 1979;70:3300. doi: 10.1063/1.437915.

18. Swanson SD, Malyarenko DI, Fabiilli ML, Welsh RC, Nielsen J-F, Srinivasan A. Molecular, dynamic, and structural origin of inhomogeneous magnetization transfer in lipid membranes: Origin of ihMT Contrast. Magn. Reson. Med. 2016:n/a-n/a. doi: 10.1002/mrm.26210.

19. Prevost VH, Girard OM, Varma G, Alsop DC, Duhamel G. Minimizing the effects of magnetization transfer asymmetry on inhomogeneous magnetization transfer (ihMT) at ultra-high magnetic field (11.75 T). Magn. Reson. Mater. Phys. Biol. Med. 2016;29:699–709. doi: 10.1007/s10334-015-0523-2.

20. Varma G, Girard OM, Prevost VH, Grant AK, Duhamel G, Alsop DC. In vivo measurement of a new source of contrast, the dipolar relaxation time, T_{1D}, using a modified inhomogeneous magnetization transfer (ihMT) sequence: In Vivo Measurement of T_{1D} Using ihMT. Magn. Reson. Med. [Internet] 2016. doi: 10.1002/mrm.26523.

21. Malyarenko DI, Zimmermann EM, Adler J, Swanson SD. Magnetization transfer in lamellar liquid crystals: Lamellar LC as Model MT Systems. Magn. Reson. Med. 2014;72:1427–1434. doi: 10.1002/mrm.25034.

22. Pampel A, Müller DK, Anwander A, Marschner H, Möller HE. Orientation dependence of magnetization transfer parameters in human white matter. NeuroImage 2015;114:136–146. doi: 10.1016/j.neuroimage.2015.03.068.

23. Yarnykh VL. Fast macromolecular proton fraction mapping from a single off-resonance magnetization transfer measurement. Magn. Reson. Med. 2012;68:166–178. doi: 10.1002/mrm.23224.

24. O'Brien JS, Sampson EL. Lipid composition of the normal human brain: gray matter, white matter, and myelin. J. Lipid Res. 1965;6:537–544.

25. Baumann N, Bourre JM, Jacque C, Harpin ML. Lipid composition of quaking mouse myelin: comparison with normal mouse myelin in the adult and during development. J. Neurochem. 1973;20:753–759. doi: 10.1111/j.1471-4159.1973.tb00036.x.

26. Hogan EL, Joseph KC. Composition of cerebral lipids in murine leucodystrophy: the quaking mutant. J. Neurochem. 1970;17:1209–1214. doi: 10.1111/j.1471-4159.1970.tb03370.x.

27. Horrocks LA. Composition of mouse brain myelin during development. J. Neurochem. 1968;15:483–488.

28. O'Brien JS, Sampson EL. Fatty acid and fatty aldehyde composition of the major brain lipids in normal human gray matter, white matter, and myelin. J. Lipid Res. 1965;6:545–551.

29. Lodish H, Berk A, Zipursky S. Section 5.3, Biomembranes: Structural Organization and Basic Functions. In: Molecular Cell Biology. 4th edition. New York: W. H. Freeman; 2000.

30. Mateu L, Morán O, Padrón R, Borgo M, Vonasek E, Márquez G, Luzzati V. The action of local anesthetics on myelin structure and nerve conduction in toad sciatic nerve. Biophys. J. 1997;72:2581–2587. doi: 10.1016/S0006-3495(97)78901-X.

31. Kucharczyk W, Macdonald PM, Stanisz GJ, Henkelman RM. Relaxivity and magnetization transfer of white matter lipids at MR imaging: importance of cerebrosides and pH. Radiology 1994;192:521–529. doi: 10.1148/radiology.192.2.8029426.

32. Mossahebi P, Yarnykh VL, Samsonov A. Analysis and correction of biases in cross-relaxation MRI due to biexponential longitudinal relaxation: Modified Cross-Relaxation Imaging (mCRI). Magn. Reson. Med. 2014;71:830–838. doi: 10.1002/mrm.24677.

33. Deloire-Grassin MSA, Brochet B, Quesson B, Delalande C, Dousset V, Canioni P, Petry KG. In vivo evaluation of remyelination in rat brain by magnetization transfer imaging. J. Neurol. Sci. 2000;178:10–16.

34. Lemaire L, Franconi F, Saint-Andre JP, Roullin VG, Jallet P, Le Jeune JJ. High-field quantitative transverse relaxation time, magnetization transfer and apparent water diffusion in experimental rat brain tumour. NMR Biomed. 2000;13:116–123.

35. Natt O, Watanabe T, Boretius S, Frahm J, Michaelis T. Magnetization transfer MRI of mouse brain reveals areas of high neural density. Magn. Reson. Imaging 2003;21:1113–1120. doi: 10.1016/j.mri.2003.08.012.

36. Kuo Y-T, Herlihy AH, So P-W, Bhakoo KK, Bell JD. In vivo measurements of T1 relaxation times in mouse brain associated with different modes of systemic administration of manganese chloride. J. Magn. Reson. Imaging 2005;21:334–339. doi: 10.1002/jmri.20285.

37. Watanabe T, Frahm J, Michaelis T. Myelin mapping in the central nervous system of living mice using contrast-enhanced magnetization transfer MRI. NeuroImage 2012;63:812–817. doi: 10.1016/j.neuroimage.2012.06.073.

38. Watanabe T, Frahm J, Michaelis T. Myelin mapping in the living mouse brain using manganese-enhanced magnetization transfer MRI. NeuroImage 2010;49:1200–1204. doi: 10.1016/j.neuroimage.2009.09.050.

39. Naumova AV, Akulov AE, Khodanovich MY, Yarnykh VL. High-resolution three-dimensional macromolecular proton fraction mapping for quantitative neuroanatomical imaging of the rodent brain in ultra-high magnetic fields. NeuroImage 2016. doi: 10.1016/j.neuroimage.2016.09.036.

40. Varma G, Schlaug G, Alsop DC. 3D Acquisition of the Inhomogeneous Magnetization Transfer Effect for Greater White Matter Contrast. In: International Society for Magnetic Resonance in Medicine. Salt Lake City, Utah, USA; 2013. p. 4224.

41. Girard OM, Le Troter A, Varma G, Prevost VH, Guye M, Ranjeva J-P, Alsop DC, Duhamel G. Whole Brain inhomogeneous MT using an ihMT prepared 3D GRE sequence at 1.5T. In: International Society for Magnetic Resonance in Medicine. Milan, Italy; 2015. p. 4236.

Table 1. Saturation parameters varied in optimization experiments.

Variable Parameter		Parameter Value				
		Δf (kHz)	$B_{1,RMS}$ (μT)	$PW/\Delta t$ (ms/ms)	τ (s)	E_{TR} ($\mu T^2.s$)
Fig. 4	Δf	6 ; 8 ; 10 ; 12 ; 14 ; 16 ; 18 ; 20	5.1 ; 6.7 ; 8.4	3/3.3	0.9	23 ; 40 ; 60
Fig. 5a	PW	10	6.7	1/3.3 ; 2/3.3 ; 3/3.3	0.9	40
Fig. 5b	$(PW,\Delta t)$	10	6.7	1/1.3 ; 2/2.3 ; 3/3.3	0.9	40
Fig. 5c	$B_{1,RMS}$	10	2.4 ; 3.3 ; 4.7 ; 5.8 ; 6.7 ; 7.4	3/3.3	0.9	5 ; 10 ; 20 ; 30 ; 40 ; 50
Fig. 5d	τ	10	6.7	3/3.3	0.25; 0.5; 0.7; 0.9; 1.1; 1.3	11 ; 22 ; 31 ; 40 ; 49 ; 58

Table 2. Quantitative ihMTR and MTR values in mouse CNS.

IhMTR and MTR values measured in CNS structures indicated in Figure 6. Values are reported as mean±group standard deviation (N=4 animals)

(a) measured on axial images;
(c) measured on coronal images;
(s) measured on sagittal images;
(a-c) mean of measurements on axial and coronal images;
(c-s) mean of measurements on coronal and sagittal images;
(a-c-s) mean of measurements on axial, coronal and sagittal images;

			mean ihMTR (%) ± group standard deviation	**mean MTR (%)** ± group standard deviation
White matter	**SCWM**	*(s)*	**5.4±0.2**	**40.3±3.2**
	IC	*(a)*	**4.9±0.3**	**44.5±0.7**
	TN	*(a)*	**4.8±0.2**	**43.6±1.0**
	Fo	*(s)*	**4.1±0.4**	**40.9±1.3**
	Fi	*(c)*	**4.0±0.2**	**39.3±0.7**
	CC	*(a-c-s)*	**3.9±0.2**	**40.9±0.4**
	Ce	*(c-s)*	**3.4±0.1**	**43.6±1.3**
	EC	*(a-c)*	**3.3±0.2**	**42.6±1.0**
Mixed	**BS**	*(s)*	**5.2±0.3**	**43.6±1.7**
	Tha	*(s)*	**3.3±0.2**	**41.7±1.0**
Gray Matter	**SCGM**	*(s)*	**4.1±0.2**	**39.8±3.3**
	Co	*(c-s)*	**3.6±0.2**	**42.6±1.2**
	CPU	*(c)*	**3.4±0.2**	**41.1±1.0**
	cGM	*(a)*	**2.4±0.2**	**41.4±0.4**
	Muscle	*(a)*	**1.3±0.2**	**60.3±0.6**

Table 3. Relative ihMTR contrasts and error estimate in mouse CNS

Relative ihMTR contrasts between 2 structures are defined as the ratio of ihMTR values of 2 structures. E.g. (in bold): ihMTR contrast between IC and Mu is 3.8; 2.0 between IC and cGM; 1.9 between cGM and Mu and 1.3 between SCWM and SCGM.

			GM				Mixed		WM							
		Muscle	cGM	CPU	Co	SCGM	Tha	Bs	EC	Ce	CC	Fi	Fo	TN	IC	SCWM
	Muscle		**1.9 ± .3**	2.6 ± .3	2.8 ± .3	3.2 ± .3	2.6 ± .3	4.0 ± .3	2.5 ± .3	2.6 ± .3	3.0 ± .3	3.1 ± .3	3.2 ± .3	3.7 ± .3	**3.8 ± .3**	4.2 ± .3
GM	cGM			1.4 ± .1	1.5 ± .1	1.7 ± .1	1.4 ± .1	2.2 ± .2	1.4 ± .1	1.4 ± .1	1.6 ± .1	1.7 ± .1	1.7 ± .2	2.0 ± .1	**2.0 ± .2**	2.3 ± .1
GM	CPU				1.1 ± .1	1.2 ± .1	1.0 ± .1	1.5 ± .1	1.0 ± .1	1.0 ± .0	1.1 ± .1	1.2 ± .1	1.2 ± .1	1.4 ± .1	1.4 ± .1	1.6 ± .1
GM	Co					1.1 ± .1	0.9 ± .1	1.4 ± .1	0.9 ± .1	0.9 ± .0	1.1 ± .1	1.1 ± .1	1.1 ± .1	1.3 ± .1	1.4 ± .1	1.5 ± .1
GM	SCGM						0.8 ± .1	1.3 ± .1	0.8 ± .1	0.8 ± .0	1.0 ± .1	1.0 ± .1	1.0 ± .1	1.2 ± .1	1.2 ± .1	**1.3 ± .1**
Mixed	Tha							1.6 ± .1	1.0 ± .1	1.0 ± .0	1.2 ± .1	1.2 ± .1	1.2 ± .1	1.5 ± .1	1.5 ± .1	1.6 ± .1
Mixed	Bs								0.6 ± .0	0.7 ± .0	0.8 ± .0	0.8 ± .0	0.8 ± .1	0.9 ± .0	0.9 ± .1	1.0 ± .0
WM	EC									1.0 ± .0	1.2 ± .1	1.2 ± .1	1.2 ± .1	1.5 ± .1	1.5 ± .1	1.6 ± .1
WM	Ce										1.1 ± .1	1.2 ± .1	1.2 ± .1	1.4 ± .1	1.4 ± .1	1.6 ± .1
WM	CC											1.0 ± .1	1.1 ± .1	1.2 ± .1	1.3 ± .1	1.4 ± .1
WM	Fi												1.0 ± .1	1.2 ± .1	1.2 ± .1	1.4 ± .1
WM	Fo													1.2 ± .1	1.2 ± .1	1.3 ± .1
WM	TN														1.0 ± .1	1.1 ± .1
WM	IC															1.1 ± .1
WM	SCWM															

Acknowledgments

The authors thank Nathalie Cuge for animal handling.

Figure Legends

Fig 1. **Pulsed ihMT saturation preparation**. **(a)** Single frequency-offset (+Δf) saturation, **(b)** Cosine-Modulated pulses for simultaneous dual frequency-offset (+Δf/-Δf) saturation. **(c)** Frequency alternating pulsed approach for dual frequency-offset saturation.

Fig 2. ***In vitro* T_{1D}-filtered ihMT imaging**. **a)** ihMT images (in a.u.) obtained in long-T_{1D} hc (up) and short-T_{1D} agarose 4% (bottom) for dual frequency-offset saturation achieved with cosine-modulated pulses (CM, first image from the left) and for frequency alternating pulses with increasing values of Δt. **b)** Corresponding ihMTR values measured in hc (red curve, scale ranging from 0-50%) and agarose 4% (black curve, scale ranging from 0-5%). Error bars correspond to in-ROI standard deviation. Other saturation parameters were $PW=1.0ms$, $\tau=0.9s$, $B_{1,RMS}=6.7\mu T$ and $\Delta f=10\ kHz$.

Fig 3. ***In vivo* T_{1D}-filtered ihMT imaging**. **a)** M_0 image including location of IC, cGM and Mu structures (up left). Typical mouse brain T_{1D} map (bottom left) obtained using the method described in (20) and showing long T_{1D} values in WM, GM structures and short T_{1D} values in muscle. IhMTR images (in %) obtained for dual frequency-offset saturation achieved with cosine-modulated pulses (CM) and for frequency alternating pulses with increasing values of Δt are shown on the right. **b)** Quantitative ihMTR values measured in IC (red curve), cGM (orange curve) and Mu (green curve) and **c-d)** corresponding ihMTR contrasts and CNR (between IC and Mu – blue curve, cGM and Mu – black curve and IC and cGM – red curve). Error bars correspond to group (N=3) standard deviation. Other saturation parameters were $PW=1.0ms$, $\tau=0.9s$, $B_{1,RMS}=6.7\mu T$ and $\Delta f=10\ kHz$.

Fig 4. **Sensitivity optimization (effect of frequency offset)**. Variation of ihMTR values (in %) with frequency offset Δf (in kHz) in IC **(a)**, CC **(b)**, cGM **(c)** and Mu **(d)** for different values of $B_{1,RMS}$. Error bars correspond to group (N=3) standard deviation. Other saturation parameters were $PW/\Delta t$=3/3.3ms and τ=0.9s.

Fig 5. Sensitivity optimization (effects of RF saturation pulses). Variations of ihMTR values in IC (red curves), cGM (orange curves) and Mu (green curves) with *PW* **(a)**, Δt **(b)**, $B_{1,RMS}$ **(c)** and τ **(d)**. The frequency offset was set to 10kHz and other saturation parameters were $\Delta t=3.3ms$, $\tau=0.9s$ and $B_{1,RMS}=6.7\mu T$ in **(a)**, $\tau=0.9s$ and $B_{1,RMS}=6.7\mu T$ in **(b)**, $PW/\Delta t=3.0/3.3ms$ and $\tau=0.9s$ in **(c)** $PW/\Delta t=3.0/3.3ms$ and $B_{1,RMS}=6.7\mu T$ in **(d)**. Error bars correspond to group (N=3) standard deviation.

Fig 6. **Optimized ihMT mouse CNS images**. MT^{+}, MTR and ihMTR images obtained with $PW/\Delta t=3.0/3.3ms$, $\Delta f=10kHz$, $B_{1,RMS}=6.7\mu T$ and $\tau=0.9s$ in axial, coronal and sagittal directions. Brain CNS structures where ihMTR and MTR values were measured are indicated in the MT^{+} images.

Supplementary Material

Fig. S1. Effect of Magnetic field strength on ihMT signal. **(a)** M_0 and ihMT images obtained at 1.5T (up) and 11.75T (bottom) in the same conditions of temperature (25°C) and saturation parameters on a phantom composed of 2 different hair conditioner samples (*hc1, hc2*) and gadolinium-doped (2mM) water (H_2O*). The 2D ihMT RARE sequence described in the Material and Methods section was used at 11.75T, and the sequence optimized for human and described in (3), was used at 1.5T. **(b-e)** Variations of ihMTR in *hc1, hc2* and H_20* at 1.5T (plain marks) and 11.75T (open marks) and as a function of Δf **(b)**, $B_{1,RMS}$ **(c)**, τ **(d)** and Δt **(e)**. Other saturation parameters were $PW/\Delta t=1.0/2.0ms$, $\tau=1s$ and $B_{1,RMS}=5.5\mu T$ in **(b)**, $PW/\Delta t=1.0/2.0ms$, $\tau=1s$ and $\Delta f=10\ kHz$ in **(c)**, $PW/\Delta t=1.0/2.0ms$ and $\Delta f=10\ kHz$ in **(d)**, $PW=1.0ms$, $B_{1,RMS}=5.5\mu T$, $\tau=1s$ and $\Delta f=10\ kHz$ in **(e)**. As expected, doped-water did not show any ihMT signal at both field strengths. For all configurations (except hc1, 4kHz data point in b), attributed to noise variance), absolute ihMTR values were systematically slightly higher at 11.75T compared to that at 1.5T. However, the dynamics of ihMTR was mostly independent of the magnetic field as demonstrated by the similar variations of ihMTR with the saturation parameters values.

top

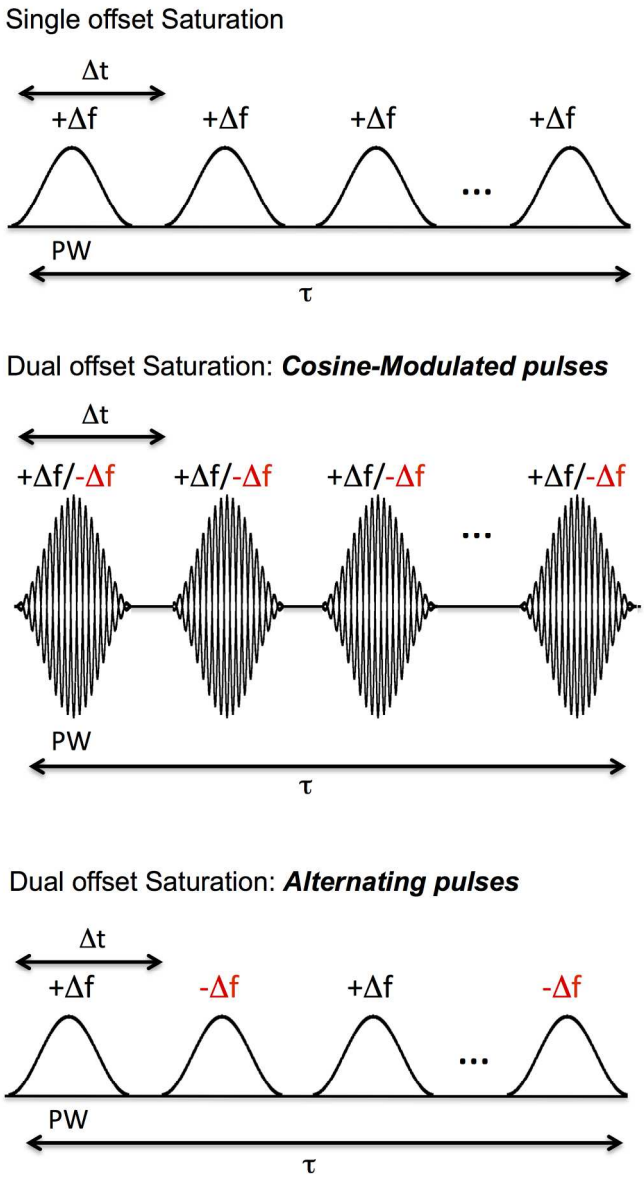

Fig. 1

Figure 1:Pulsed ihMT saturation preparation. (a) Single frequency-offset (+Δf) saturation, (b) Cosine-Modulated (CM) pulses for simultaneous dual frequency-offset (+Δf/-Δf) saturation. (c) Frequency alternating pulsed approach for dual frequency-offset saturation.

177x234mm (300 x 300 DPI)

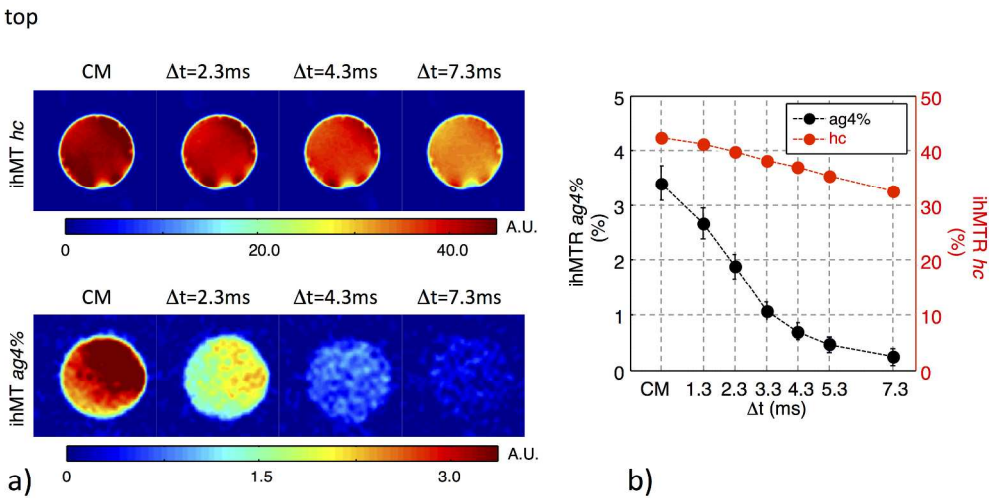

Fig. 2

Fig 2: In vitro T1D-filtered ihMT imaging. a) ihMT images (in a.u.) obtained in long-T1D hc (up) and short-T1D agarose 4% (bottom) for dual frequency-offset saturation achieved with cosine-modulated pulses (CM, first image from the left) and for frequency alternating pulses with increasing values of Δt. b) Corresponding ihMTR values measured in hc (red curve, scale ranging from 0-50%) and agarose 4% (black curve, scale ranging from 0-5%). Error bars correspond to in-ROI standard deviation. Other saturation parameters were PW=1.0ms, τ=0.9s, B1,RMS=6.7μT and Δf=10 kHz.

261x151mm (300 x 300 DPI)

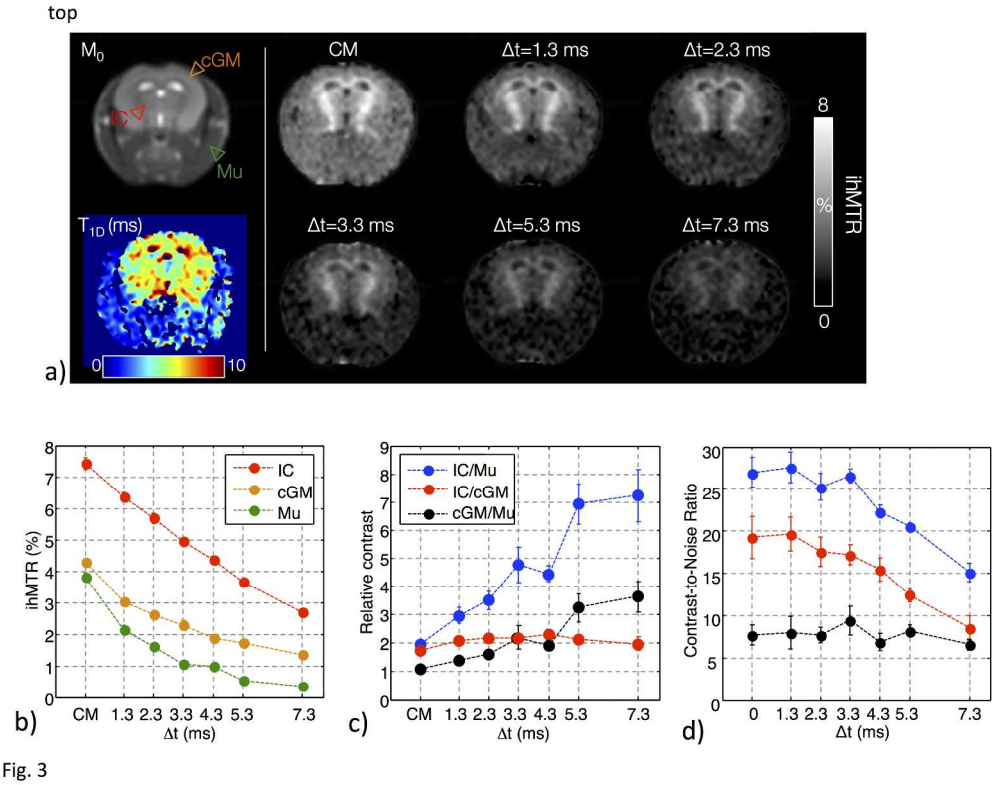

Fig. 3

Fig 3. In vivo T1D-filtered ihMT imaging. a) M0 image including location of IC, cGM and Mu structures (up left). Typical mouse brain T1D map (bottom left) obtained using the method described in (20) and showing long T1D values in WM, GM structures and short T1D values in muscle. IhMTR images (in %) obtained for dual frequency-offset saturation achieved with cosine-modulated pulses (CM) and for frequency alternating pulses with increasing values of Δt are shown on the right. b) Quantitative ihMTR values measured in IC (red curve), cGM (orange curve) and Mu (green curve) and c-d) corresponding ihMTR contrasts and CNR (between IC and Mu – blue curve, cGM and Mu – black curve and IC and cGM – red curve). Error bars correspond to group (N=3) standard deviation. Other saturation parameters were PW=1.0ms, τ=0.9s, B1,RMS=6.7μT and Δf=10 kHz.

296x234mm (300 x 300 DPI)

top

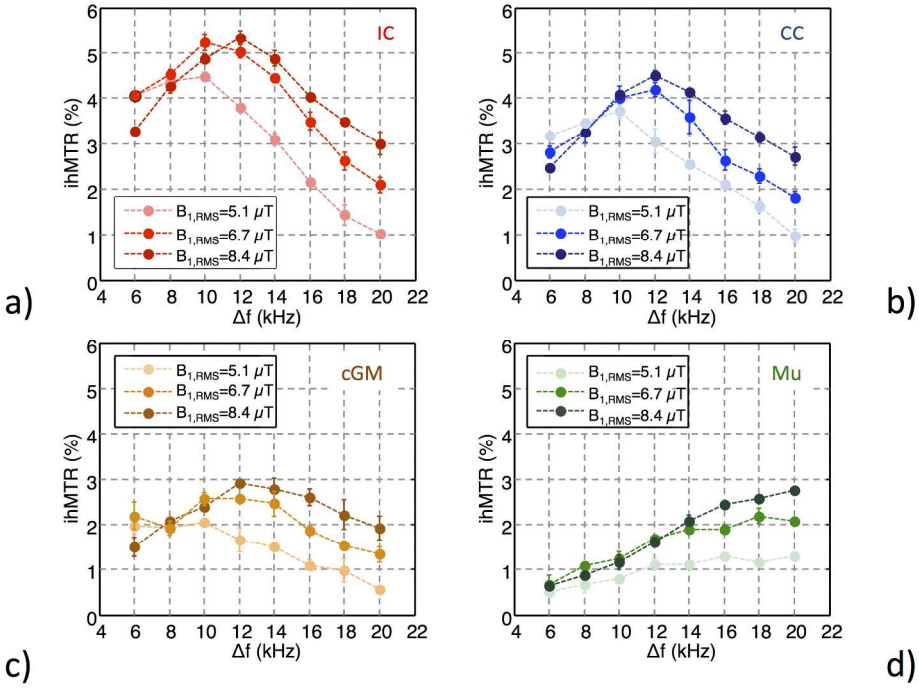

Fig. 4

Figure 4: Sensitivity optimization (effect of frequency offset). Variation of ihMTR values (in %) with frequency offset Δf (in kHz) in IC (a), CC (b), cGM (c) and Mu (d) for different values of $B_{1,RMS}$. Error bars correspond to group (N=3) standard deviation. Other saturation parameters were PW/Δt=3/3.3ms and τ=0.9s.

223x180mm (300 x 300 DPI)

top

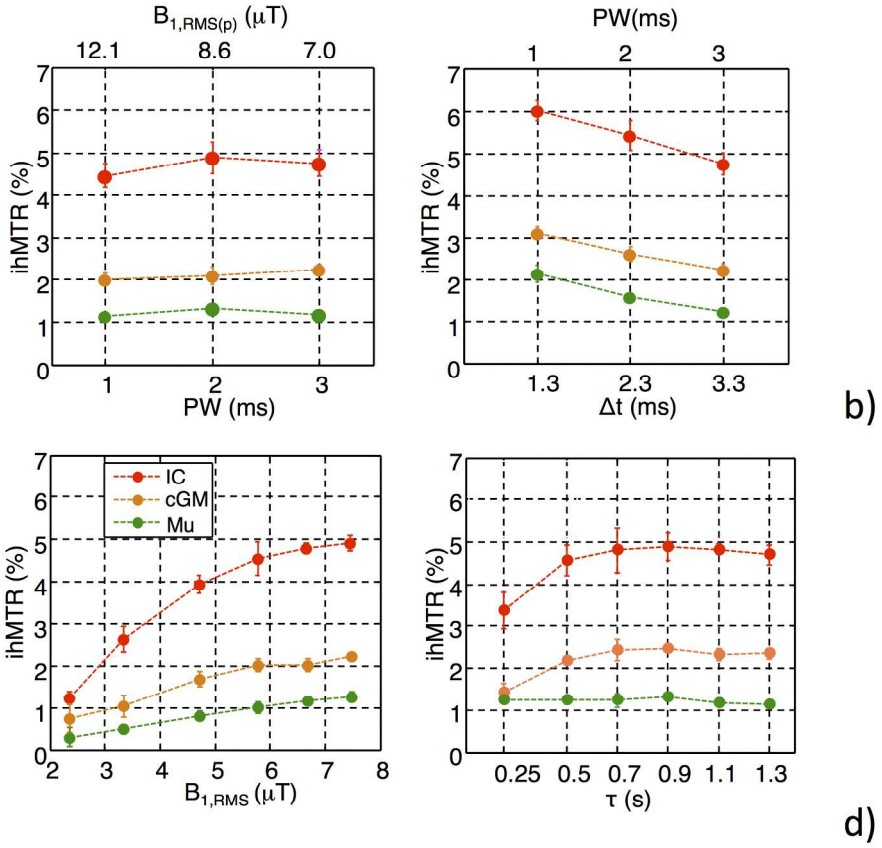

Fig. 5

Figure 5: Sensitivity optimization (effects of RF saturation pulses). Variations of ihMTR values in IC (red curves), cGM (orange curves) and Mu (green curves) with PW (a), Δt (b), $B_{1,RMS}$ (c) and τ (d). The frequency offset was set to 10kHz and other saturation parameters were Δt=3.3ms, τ=0.9s and $B_{1,RMS}$=6.7μT in (a), τ=0.9s and $B_{1,RMS}$=6.7μT in (b), PW/Δt=3.0/3.3ms and τ=0.9s in (c) PW/Δt=3.0/3.3ms and $B_{1,RMS}$=6.7μT in (d). Error bars correspond to group (N=3) standard deviation

206x197mm (300 x 300 DPI)

top

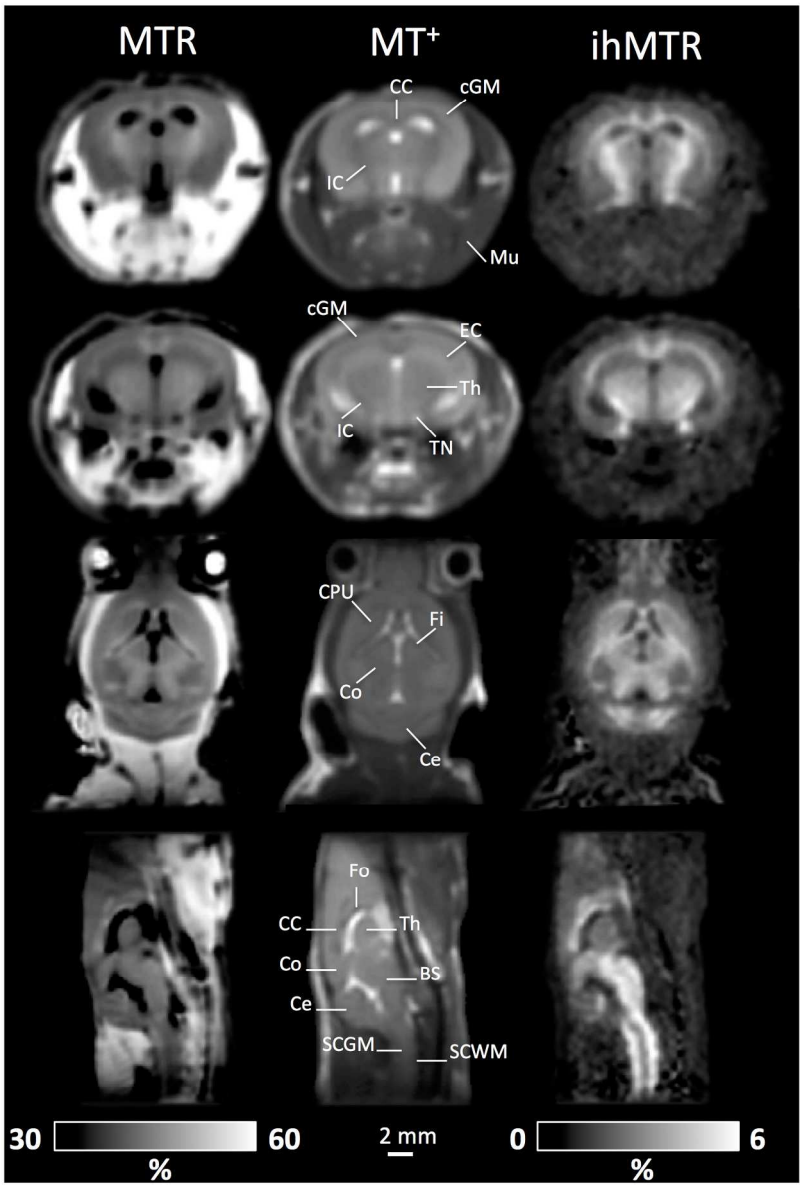

Fig. 6

Figure 6: Optimized ihMT mouse CNS images. MT^+, MTR and ihMTR images obtained with PW/Δt=3.0/3.3ms, Δf=10kHz, $B_{1,RMS}$=6.7μT and τ=0.9s in axial, coronal and sagittal directions. Brain CNS structures where ihMTR and MTR values were measured are indicated in the MT^+ images.

185x238mm (300 x 300 DPI)

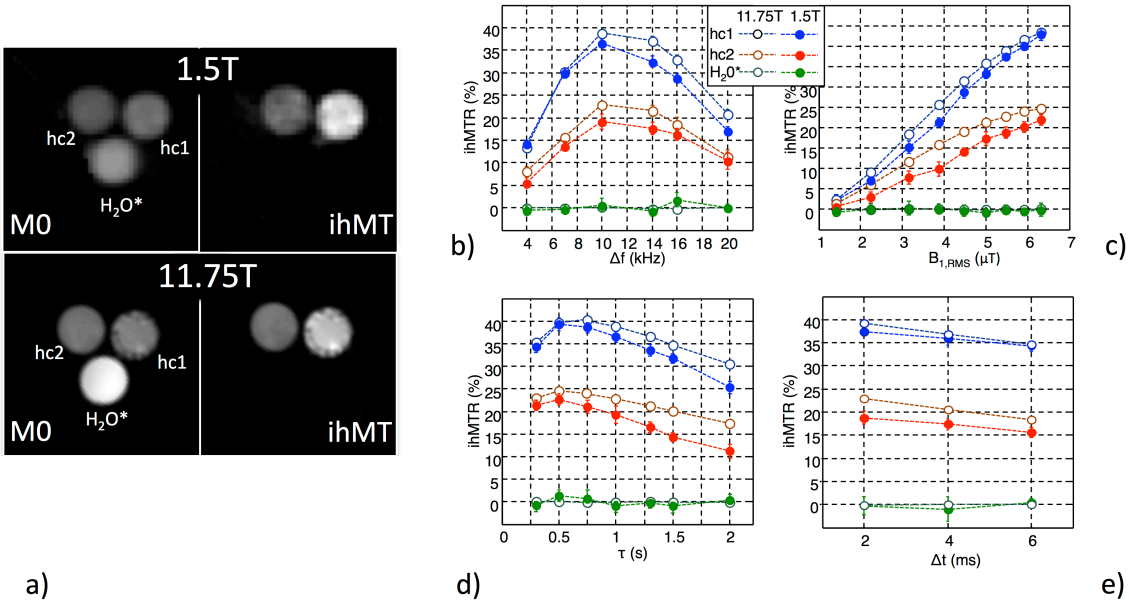

Fig S1. Effect of Magnetic field on ihMT. **(a)** M_0 and ihMT images obtained at 1.5T (up) and 11.75T (bottom) in the same conditions of temperature (25°C) and saturation parameters on a phantom composed of 2 different hair conditioner samples (*hc1, hc2*) and gadolinium-doped (2mM) water (H_2O*). The 2D ihMT RARE sequence described in the Material and Methods section was used at 11.75T, and the sequence optimized for human and described in [3], was used at 1.5T. **(b-e)** Variations of ihMTR in *hc1, hc2* and H_20* at 1.5T (plain marks) and 11.75T (open marks) and as a function of Δf **(b)**, $B_{1,RMS}$ **(c)**, τ **(d)** and Δt **(e)**. Other saturation parameters were $PW/\Delta t=1.0/2.0ms$, $\tau=1s$ and $B_{1,RMS}=5.5\mu T$ in **(b)**, $PW/\Delta t=1.0/2.0ms$, $\tau=1s$ and $\Delta f=10$ *kHz* in **(c)**, $PW/\Delta t=1.0/2.0ms$ and $\Delta f=10$ *kHz* in **(d)**, $PW=1.0ms$, $B_{1,RMS}=5.5\mu T$, $\tau=1s$ and $\Delta f=10$ *kHz* in **(e)**. As expected, doped-water did not show any ihMT signal at both field strengths. For all configurations (except hc1, 4kHz data point in b), attributed to noise variance), absolute ihMTR values were systematically slightly higher at 11.75T compared to that at 1.5T. However, the dynamics of ihMTR was mostly independent of the magnetic field as demonstrated by the similar variations of ihMTR with the saturation parameters values.

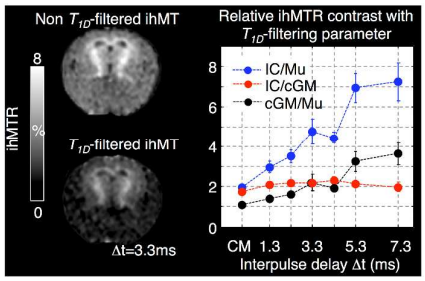

A strategy based on filtering the signal of short T_{1D} components was used to optimize the ihMT contrast for long T_{1D} myelinated structures in mouse. Typical ihMTR values on the order of 4-5% in WM, 2.5% in GM and 1-1.3% in muscle were obtained, thus leading to high positive relative ihMTR contrasts between myelinated tissues and other tissues. Of particular importance, the relative ihMTR contrast between WM and GM (~ 2) appeared to be relatively independent of the saturation parameters.

Optimization of inhomogeneous Magnetization Transfer (ihMT) MRI contrast for preclinical studies using dipolar relaxation time (T_{1D}) filtering

V.H. Prevost[1], O.M. Girard[1], S. Mchinda[1], G. Varma[2], D.C. Alsop[2] and G. Duhamel[1*]